Studies of the Large-Scale Structure in Turbulent Boundary Layers Using Simultaneous Velocity-Wavefront Measurements

Stanislav Gordeyev[1]

Department of Aerospace and Mechanical Engineering,
University of Notre Dame, Notre Dame, IN 46556

and

Adam E. Smith[2]

MZA Associates Corporation
Dayton, Ohio 45430

Simultaneous velocity field and optical distortions along the wall-normal direction were performed in a subsonic boundary layer. Comparison between wavefronts and the ones predicted using instantaneous Strong Reynolds Analogy had shown that instantaneous SRA is valid most of the time. Conditional velocity analysis had shown that positive OPD distortions are created by predominantly ejection-type Q2 events near the wall and overall uv-Reynolds shear stress is larger near the wall and smaller away from the wall. The negative distortions are mostly due to sweep-type Q4 events near the middle of the boundary layer, with significantly larger uv-Reynolds shear stress throughout the boundary layer. Conditional velocity fields during the events, where the instantaneous SRA failed to predict optical distortions, were extracted and analyzed and possible reasons for these differences are presented and discussed.

I.   Introduction

Large-scale structures, located in the outer part of the subsonic boundary layer, bear an important role in boundary layer dynamics such as the entrainment process and, via a link with small-scale structures near the wall, instantaneous drag near the wall, to mention a few [1]. While there exists a large body of experimental research about the large-scale structures [2], there are open questions about their topology, dynamics and the interaction with the near-wall structures.

Traditionally, large-scale structures are characterized by the velocity field, which is measured using hot-wires or a PIV technique. These techniques give either detailed temporal information in a few spatial points (hot-wires) or potentially time-resolved spatial velocity field information in a plane (particle image velocimetry, PIV). In order to get instantaneous three-dimensional information about the structure, one has to resort to rather complex techniques, like tomographic-PIV [3] or plenoptic [4] techniques, for example.

An alternative way to non-intrusively study the characteristics of large-scale structures in boundary layers is to measure related density distortions. Turbulent density fluctuations that are present in the region immediately around an aerodynamic vehicle alter the local speed of light passing into and/or out of the aircraft through the turbulent region. This phenomenon is known as

---

[1] Research Associate Professor, Department of Mechanical and Aerospace Engineering, Hessert Laboratory for Aerospace Research, Notre Dame, IN 46556, AIAA Associate Fellow.
[2] Research Scientist, MZA Associates Corporation, 1360 Technology Ct., Suite 200, Dayton, OH 45430, AIAA Student Member.

the aero-optic problem [5]. As planar wavefronts propagate through these unsteady density distributions, they get distorted. These distortions can be accurately measured by various wavefront sensors. The levels of optical wavefront distortions can be quantified by the Optical-Path-Difference, OPD(x,z,t), [5]

$$OPD(x,z,t) = K_{GD}\int \rho'(x,y,z,t)dy, \tag{1}$$

where K_{GD} is the Gladstone-Dale constant and the integration is performed along the beam propagation axis, y. Sutton [6] introduced the so-called 'linking equation' relating turbulence quantities and levels of optical distortions, given as

$$OPD_{rms}^2 = 2K_{GD}^2\int \rho_{rms}^2 \Lambda_\rho(y)dy, \tag{2}$$

where OPD_{rms} is the spatial root-mean-square of the OPD, $\rho_{rms}(y)$ is the root-mean-square density fluctuation profile along the beam direction, and $\Lambda_\rho(y)$ is the density correlation length in the wall-normal direction. Using the linking equation, Eq. (2), a model for time-averaged levels of aero-optical distortions was developed and it was shown to correctly predict OPD_{rms} over a wide range of Mach numbers [7], as well as identifying the large-scale structures as main source of aero-optical distortions.

As stated before, in incompressible, wall-heated boundary layers density fluctuations occur due to total temperature variations. Above M = 0.3, compressibility effects also can change the density. If the total temperature is assumed to be a constant, which is equivalent to zero pressure fluctuations, the density fluctuations, ρ', in boundary layers are due to the static temperature fluctuations, T', (adiabatic cooling/heating) and the instantaneous version of the Strong Reynolds Analogy (SRA) [8] leads to a relationship with the velocity field,

$$CpT'(\vec{x},t) = -\overline{U}u'(\vec{x},t) \tag{3}$$

The time-averaged version of SRA was shown to correctly estimate the time-averaged levels of BL aero-optical distortions with adiabatic walls [7]. However, for non-adiabatic walls SRA was found to consistently underpredict levels of aero-optical distortions [9] and the importance of including the pressure term to properly predict aero-optical distortions was shown.

In this work, we leverage both velocimetry and optical techniques to characterize large scale structure in compressible turbulent boundary layers. A complimentary experimental technique, which uses simultaneous velocity-wavefront measurements, is proposed. To demonstrate the technique, simultaneous wavefront/velocity measurements were performed in the compressible subsonic adiabatic boundary layer. Since wavefronts are proportional to the integrated density field, the comparison between the velocity field and the wavefront would provide additional information about the large-scale structures inside the boundary layer and the effect of the local pressure fluctuations, not accounted for the SRA, can be estimated and studied. In [10] very preliminary, mostly qualitative analysis of the simultaneous velocity-wavefront measurements was performed, with encouraging results. In this paper we will present more detailed quantitative results of the analysis.

As a final remark, in [9] it was showed that if the boundary layer wall is moderately-heated relative to the freestream density, it will not modify the underlying velocity structure. Rather, moderate heating simply introduces passive temperature markers in the boundary layer that effectively amplify the amplitude of aero-optical distortions. So, the proposed technique can be used to study incompressible boundary layers as well. The validity of this approach to studying low speed (M~ 0.05) boundary layers was demonstrated in [10].

II.   Experimental Set-Up

Measurements were performed in the Hessert Transonic Wind Tunnel (TWT) at the University of Notre Dame. The Transonic Wind Tunnel is the tunnel is a continuous flow indraft wind tunnel with an inlet contraction ratio of 150:1, and a cross-section of 10 cm × 9.9 cm in the tunnel test section, which is constructed of Plexiglas. The test section was 160 cm in length from the end of the inlet to the diffuser, with optical windows installed on the upper and lower walls from 130 cm to 150 cm. Freestream velocity measured using a static pressure port just upstream of the optical window, and was held constant at U = 140 m/s for the duration of the measurements.

The optical set-up is shown in Figure 1. Full circular 2-D wavefronts, resolved in both the streamwise (x) and the spanwise (z) directions, were collected using a high-speed Shack-Hartmann wavefront sensor. The wavefront aperture was 50 mm. In order to minimize the optical effect of the upper boundary layer, a Large Eddy Break Up (LEBU) device with the streamwise length of 72 mm, was mounted parallel to the upper wall of the TBL development section at a height of 11 mm, as shown in Figure 1. This configuration was designed to reduce the level of measured optical aberrations caused by the upper TBL. The LEBU trailing edge was located 2.6 cm upstream of the start of the optical window. Analysis of the effects of LEBU devices on aero-optical environment in BL [11] showed that the LEBU device reduced the aero-optical distortions of the upper boundary layer by a factor of 1.7.
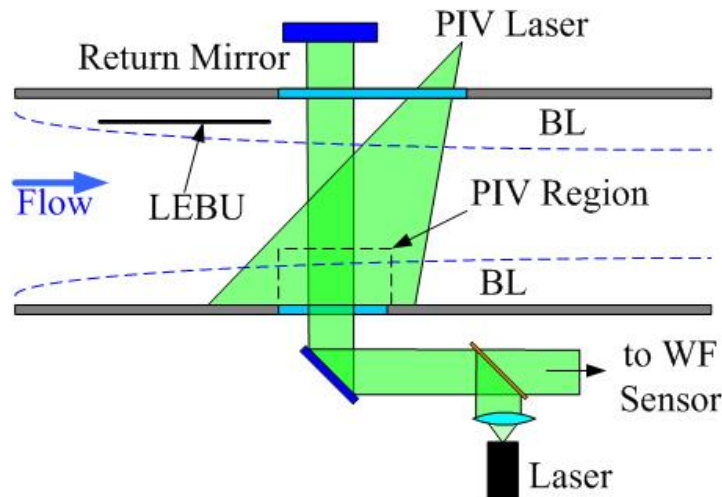

Figure 1. Schematic of the simultaneous Velocity-Wavefront measurements using PIV system and Shack-Hartmann 2-D wavefront sensor.
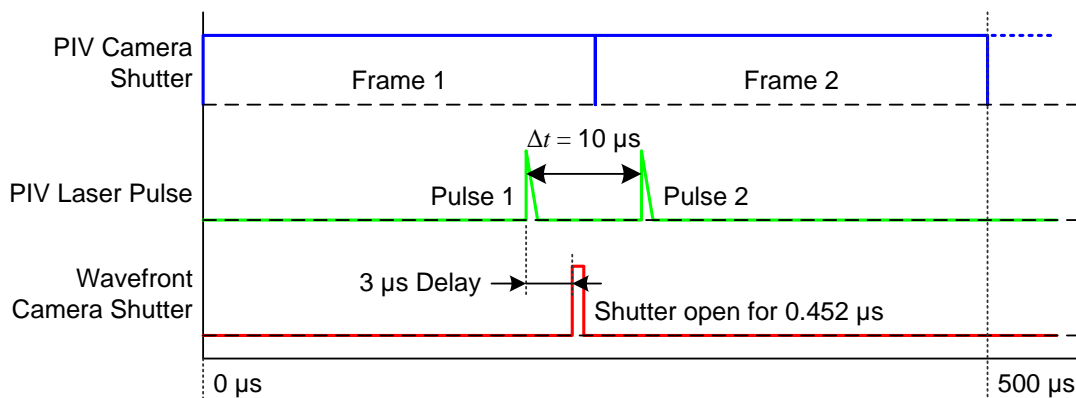
Figure 2. Timing diagram to synchronize PIV system and WaveFront Sensor.

Velocity data were acquired at a rate of 2 kHz using a commercially available 2-D PIV LaVision system in double-pulse, double-frame mode. The laser sheet was aligned along the tunnel centerline, and the frame resolution of the camera was 768×768, with a field of view of approximately 100 mm. Both PIV system and the wavefront sensor were synchronized and the timing diagram is presented in Figure 2. The time interval between laser pulses for each measurement was 10 μs. The PIV image pairs were cropped and processed in DaVis 8.2 in order to calculate the velocity vector field at intervals of 0.53 mm in the streamwise and wall-normal directions. The velocity measurements near the wall were found to be mostly corrupted due to the laser reflection off the tunnel wall, so velocity vectors below $y/\delta = 0.1$ were discarded.

Wavefront measurements with the spatial resolution of 40x40 subapertures were simultaneously acquired using a Shack-Hartmann sensor, consisted of a high-speed camera (Phantom v1611) with a mounted lenslet array, 3 μs after the first laser pulse, so as to have wavefront data that closely corresponded to each image pair used to calculate the velocity field. The shutter duration for the Shack-Hartmann sensor was only 0.452 μs long, and the points at which wavefront measurements were obtained were distributed at 1.2 mm intervals in the streamwise and spanwise directions. The aperture diameter of the wavefront beam was approximately 5 cm, with its upstream edge passing through the optical window at x = 133 cm.

Figure 3. Mean BL velocity profile in inner units. A solid line is the universal velocity profile in the log-region.

The boundary layer thickness, δ, at the measurements location was found to be approximately 15.2 mm. Integration of the velocity profiles, collected with PIV system gave δ* to be 2.2 mm and θ = 1.6 mm, giving Re_θ = 14,600 and H-factor of 1.39. Using the Clauser method, see Figure 3, the skin friction coefficient was estimated to $C_f = 2.45 \times 10^{-3}$, with a corresponding $Re_\tau = 4,170$.
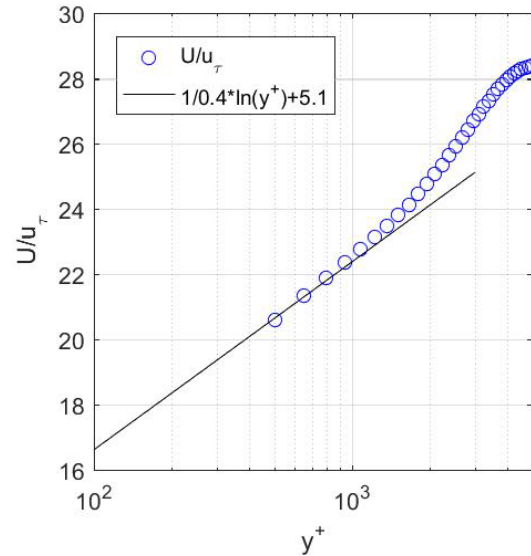
III.   Data Analysis

Wavefronts were computed using in-house software using the Southwell method [12]. Instantaneous tip/tilt and piston modes were removed from each wavefront. An example of a representative wavefront is given in Figure 4, left. The 1-D "slice" of the wavefront, OPD(x,t) = OPD$_{2D}$(x, z = const, t), along the PIV laser sheet, denoted as a dashed line in Figure 4, left, was extracted for each wavefront, shown as the black solid line in Figure 4, middle.

To check how well the instantaneous version of SRA predicts the wavefront distortions, density fluctuations were estimated from the velocity field, using Eq. (3),

$$\frac{\rho'(x,y,t)}{\rho_\infty} = -\frac{T'(x,y,t)}{T_\infty} = r(\gamma-1)M_\infty^2 \frac{\overline{U}(y)u'(x,y,t)}{U_\infty^2}. \tag{4}$$

Using Eq. (1), the density profiles were integrated in the wall-normal direction to get the velocity-related aero-optical distortions, denoted as VOPD(x,t). The velocity field is shown in Figure 4, right, and a corresponding VOPD is shown as a dashed red line in Figure 4, middle.

Once the 1-D wavefronts were computed, time-averaged spatial root-mean-squared of aero-optical distortions over the aperture, $OPD_{rms} = \left[\dfrac{1}{Ap \cdot T} \int\limits_{o}^{T} \int\limits_{Ap} OPD^2(x,t)dxdt \right]^{1/2}$, was computed from both OPD and VOPD. Also, a time-averaged error between OPD and VOPD was computed, $\varepsilon = \left[\dfrac{1}{Ap \cdot T} \int\limits_{o}^{T} \int\limits_{Ap} (OPD(x,t) - VOPD(x,t))^2 dxdt \right]^{1/2}$.
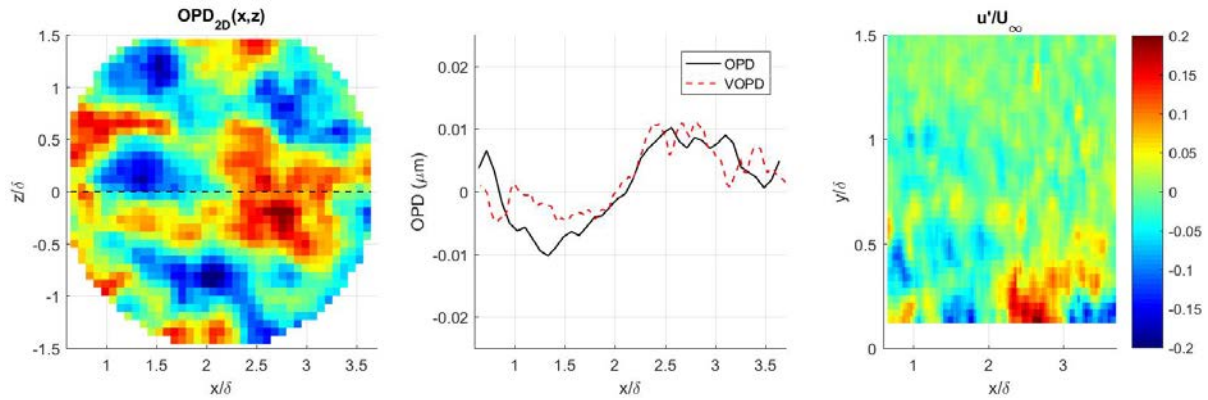

Figure 4. Left: an example of the 2-D wavefront. The location of the PIV laser sheet is indicated as a dashed line. Right: the corresponding velocity field. Middle: 1-D wavefront slice from the 2-D wavefront, OPD, and the VOPD, estimated from the velocity field.

In order to study the relation between the optical distortions and the corresponding velocity field, a conditional averaging of the instantaneous velocity field was performed for both the large positive and negative variations in OPD,

$$
\begin{aligned}
&\left\langle (u'(x,y,t),v'(x,y,t)) \,|\, OPD(x) > Th \cdot OPD_{rms} \right\rangle_x - \text{large positive OPD,}\\
&\left\langle (u'(x,y,t),v'(x,y,t)) \,|\, OPD(x) < -Th \cdot OPD_{rms} \right\rangle_x - \text{large negative OPD.}
\end{aligned}
\tag{5}
$$

Here *Th* as a threshold parameter.

Finally, instances with large differences between OPD and VOPD were selected and the corresponding conditional velocities were also extracted,

$$
\begin{aligned}
&\left\langle (u'(x,y,t),v'(x,y,t)) \,|\, (OPD(x) - VOPD(x)) > Th \cdot OPD_{rms} \right\rangle_x - \text{positive deviations,}\\
&\left\langle (u'(x,y,t),v'(x,y,t)) \,|\, (OPD(x) - VOPD(x)) < -Th \cdot OPD_{rms} \right\rangle_x - \text{negative deviations.}
\end{aligned}
\tag{6}
$$

By comparing the regions of the large local differences between the estimated and the actual wavefronts and relating them to the instantaneous velocity field allows, the validity of the instantaneous SRA can be assessed. As the estimated wavefronts rely on SRA, instances of large deviations identified from Eq. (6) should correspond to the cases where the pressure/total temperature fluctuations are not negligible.

IV.   Results

Calculations of OPD_{rms} from both OPD and VOPD gives the same value of 0.0049 microns. In [7] an analytical expression for OPD_{rms} for subsonic boundary layers was derived as a function of BL parameters and the aperture size, $OPD_{rms}(Ap) = F(Ap/\delta) \cdot 0.19 K_{GD} \rho_\infty \delta M_\infty^2 \sqrt{C_f}$

, where $F(Ap/\delta)$ is the aperture function. Substituting all the values gives the theoretical prediction for OPD_{rms} = 0.0050 microns for Ap/δ = 3.3, which agrees quite well with the experimental results. This is an expected result, as the time-averaged SRA was found to properly predict experimental results for BL aero-optical distortions for a wide range of Mach numbers up to M = 5 [7,13,14].

Spatial probability distribution for OPD is shown in Figure 5 and can be approximated fairly well as a Gaussian distribution; similar observations about the Gaussian nature of BL wavefronts were made in other experiments [15]. A spatial probability distribution of VOPD was also found to be Gaussian and is not shown here.
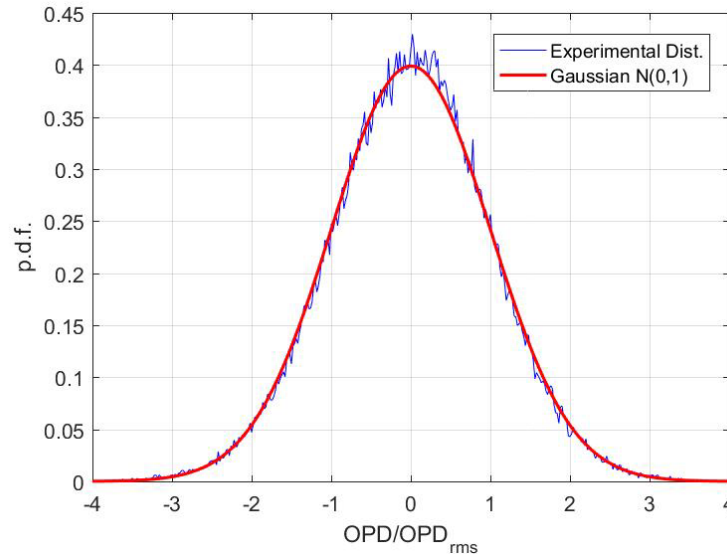

Figure 5. Experimental probability distribution of OPD and a comparison with the Gaussian distribution, $N(0,1)$.

The time-averaged error between OPD and VOPD was calculated to be ε/OPD_{rms} = 0.64. Inspection of the individual OPD and VOPD, similar to the ones in Figure 4, middle, have shown that most of the relative error comes from the larger spatial variations in VOPD as a result of noise present in PIV velocity measurements. Other sources of the differences between OPD and VOPD are due to local pressure/total temperature fluctuations; this effect will be discussed later in this paper.

A.   *Conditional velocity fields for large optical distortions*

Instantaneous version of SRA, Eq. (4), implies that the velocity-related density fluctuations depend only on the streamwise velocity fluctuations u' and positive u'-fluctuations should create positive aero-optical distortions and vice versa. To see the wall-normal distribution of the related velocity field, conditionally-calculated u' and v', Eq. (5), were time-averaged and plotted as a function of the wall-normal distance in Figure 6 for different threshold values.

Large positive OPDs, see Figure 6, right, do correspond to large positive *u*-fluctuations, consistent with the instantaneous SRA; time-averaged v-fluctuations were found to be negative and several times smaller. Most of the *u*-fluctuations are located in $y/\delta < 0.5$, with the maximum near the wall. The time-averaged conditional velocity profiles were found to be only weakly dependent on the Th-value, while the relative duration of large OPD events was significantly reduced with the increasing Th-value, from 15% for *Th* = 1 to 2% for *Th* = 2.

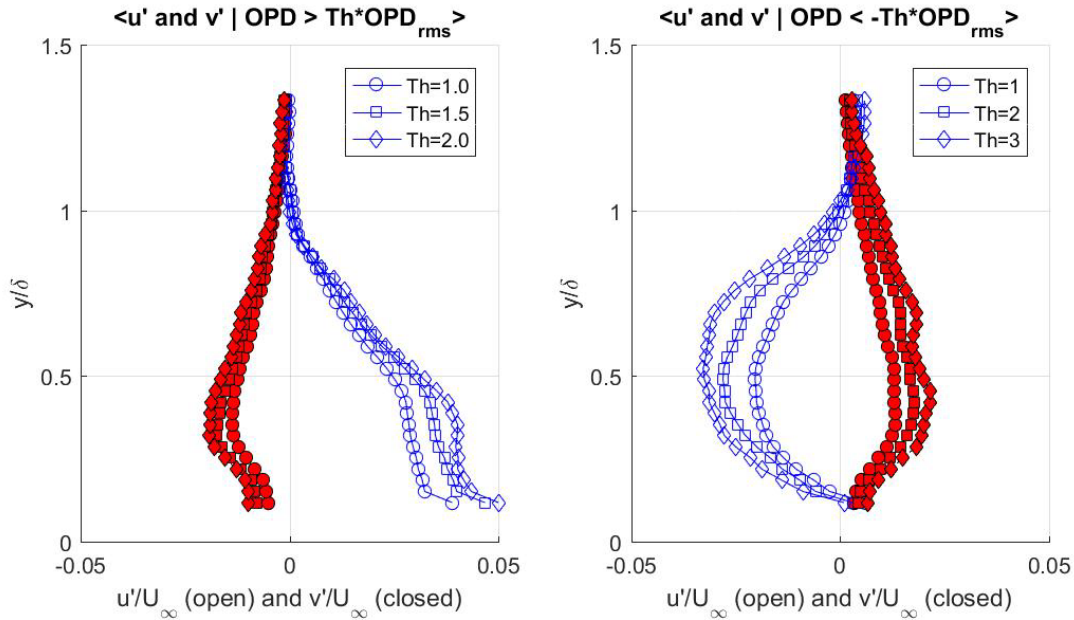Figure 6. Time-averaged wall-normal profiles of u-fluctuations (open blue symbols) and v-fluctuations (closed red symbols) for different threshold values for large positive (left) and large negative (right) OPDs.

Large negative OPDs correspond to the large negative u-fluctuations and small positive v-fluctuations, see Figure 6, right, and it is also consistent with the instantaneous SRA. The wall-normal distribution, however, is different, with the largest u-fluctuations located near the middle of the boundary layer and negligible near the wall; the v-component was also several time smaller than the u-component. So, while the optical distortions exhibit a symmetry for positive and negative fluctuations, as demonstrated in Figure 5, the related conditional velocity fields for large positive and large negative optical distortions show a significant asymmetry. It implies that the different BL structures might be responsible for these optical distortions.

To further study the conditional velocity fields, a dual distribution of both u- and v-fluctuations, known as a quadrant analysis [16], was performed at selected wall-normal locations, $y/\delta = 0.25$, 0.50 and 0.8. For un-conditional velocity fluctuations, shown in Figure 7, left column, near the wall locations $y/\delta = 0.25$ and 0.50 and, in lesser degree at $y/\delta = 0.8$, u-v-distributions are slightly skewed, with the most probable (u',v')-events been in Q4-quadrant (sweep, u'>0, v'<0 events), while ejection-type, u'<0, v'>0, events in Q2-quadrant have longer tails in the distributions. The skewness in the distribution implies asymmetry between the duration, strength and the frequency of the ejection-type and the sweep events [16].

Analysis of the conditional u-v-distributions during the large positive, Figure 7, middle column, and large negative, Figure 7, right, optical distortions also have shown asymmetry in the distributions. The u-v distributions during the positive distortions are tighter, compared to the unconditional and negative optical distortion cases, meaning that the uv-Reynolds stress, responsible to the turbulent production, is reduced during the large positive optical distortions. Also, the u-v-distributions are shifted toward Q4-quadrant during the large positive optical distortions, compared to the ones for the negative optical distortions. It means that the probability of strong ejection-type events for the positive optical events is decreased, while the strength of the sweep events is largely unchanged.
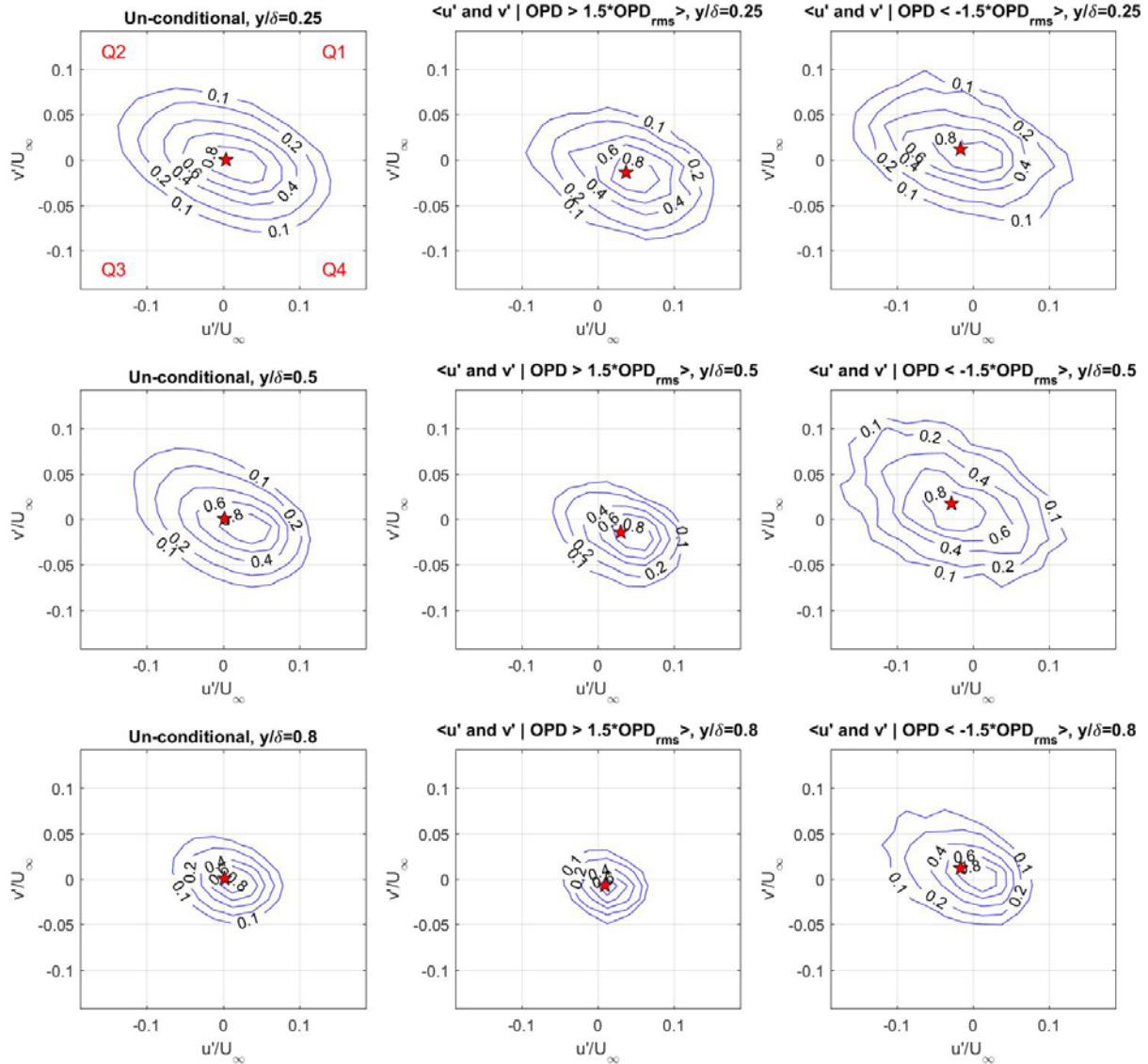

Figure 7. Dual distribution of u- and v-components for un-conditional (left column), for large positive (middle column) and negative (right column) optical distortions at different wall-normal locations. Red stars on each plot indicate averaged (u',v')-values. Th-value in Eq. (5) is 1.5. The quadrants are annotated in the top left plot.

The distribution of conditionally-averaged uv-Reynolds shear stress inside the boundary layer during the large positive and negative optical events are presented in Figure 8, along with the unconditional uv-Reynolds shear stress distribution. The Reynolds shear stress is related to the amount of the local turbulence production. Both types of optical events have a different effect on the shear stress. During the positive OPDs, the shear stress is amplified near the wall, $y/\delta <$ 0.4, and suppressed in the outer region of the boundary layer. During the negative OPDs, the shear stress is almost twice larger inside the whole boundary layer.
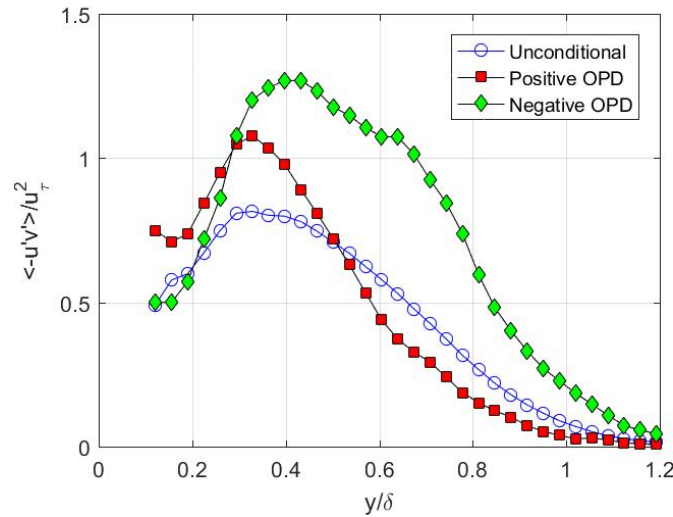

Figure 8. The wall-normal distribution of the uv-Reynolds shear stress, $\langle -u'v' \rangle / u_\tau^2$ for the unconditional case, and during large positive and negative OPDs.
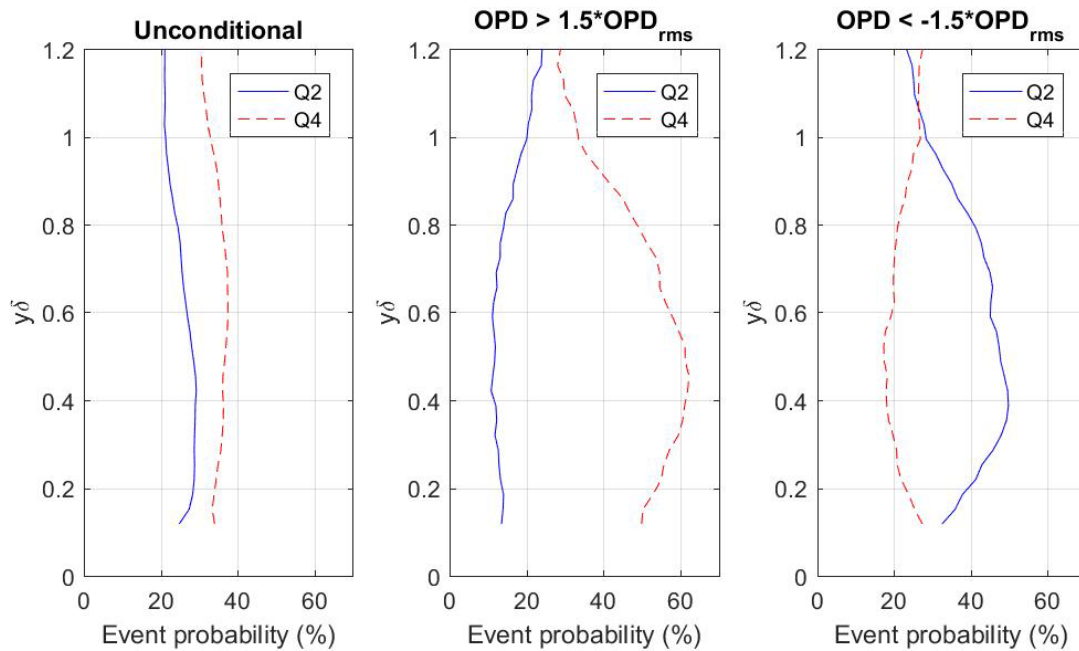

Figure 9. Wall-normal variation of relative probabilities of Q2- and Q4-events for unconditional case (left), and during large positive (middle) and negative (right) optical distortions.

The overall relative probabilities of the ejection-type (Q2) and the sweep (Q4) events can be found by integrating the probability distributions in Q2 and Q4 quadrants. Results are shown in Figure 9. For the unconditional case, the relative probability of Q4-events is approximately 35-40%, while Q2-events happen with 20-30%-probability throughout the whole boundary layer. During the large positive optical distortions, Q4-events dominate in the boundary layer with the largest 60%-probability around $y/\delta = 0.5$, and Q2-events are relatively infrequent, ~15%. During the large negative optical distortions, Q2-events happen roughly half of the time and the relative probability of Q4-events is reduced to ~20%.

In this paper, only one-dimensional wavefronts were analyzed. Once established that positive and negative optical distortions are due to different flow events or structures, analysis of 2-D dimensional distortions, see Figure 4, left, like the spanwise extent near the local minima and maxima, might provide non-intrusive optical measurements of the spanwise size of the underlying large-scale structures. For instance, from Figure 4, left, a typical spanwise extent of the negative optical distortions is found to be approximately 0.5δ with a typical streamwise extend of ~1δ; on the contrary, the spanwise extent near the positive optical distortions is larger, ~δ. Additional analysis is needed to further study this notion.

B. Conditional velocity fields during large differences between optical and velocity-predicted distortions

Conditional velocity fields were also analyzed during instances, when the actual wavefronts were either larger or smaller than the velocity-predicted ones, using Eq. (6). Results are presented in Figure 10. The conditionally-averaged u-fluctuation profiles during large positive differences, Figure 10, left, are negative and are the largest in the middle of the boundary layer, while they are positive for the positive differences, see Figure 10, right, and bigger in amplitude compared to the negative difference case; the largest u-fluctuations for the negative difference are around $y/\delta = 0.3$. Average V-fluctuations are relatively small during both types of differences. The analysis of the conditional u-v-distributions did not reveal any significant differences between the unconditional and conditional events and therefore are not presented here.
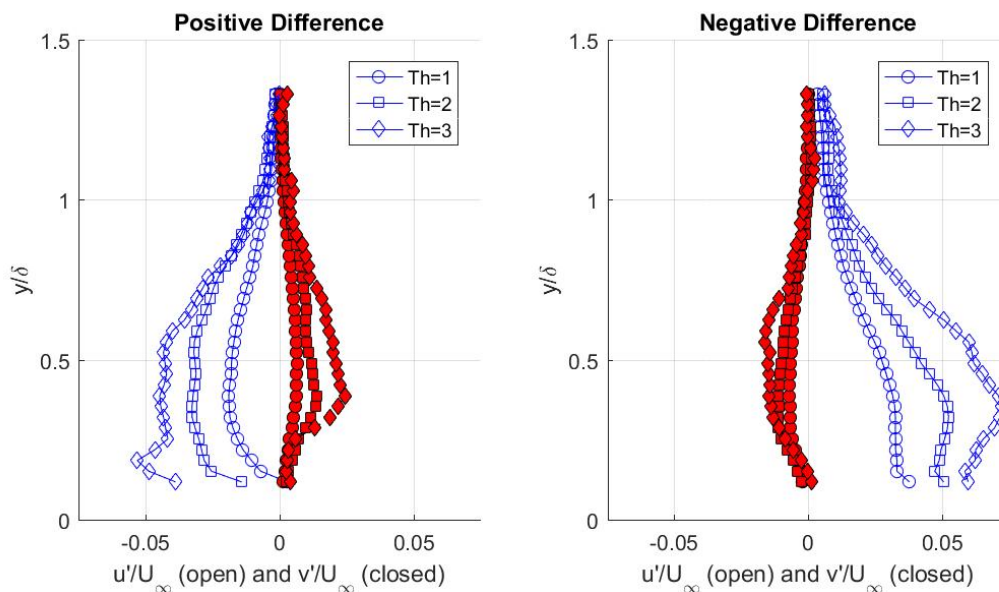
Figure 10. Conditional-averaged u- and v-fluctuation profiles for positive (left) and negative (right) differences between the measured and the velocity-predicted optical distortions, Eq. (6), for different threshold values.

The difference between the measured and actual wavefronts inside these large-scale structures arises from two sources. One of them is a contamination from the second boundary layer at the opposite wall, which was significantly reduced by LEBU device, but still present. The second boundary layer would not seriously change the overall optical distortions, so the conclusions in the previous section would be still valid. But when looking for differences between observed and SRA-predicted optical distortions, the presence of the secondary boundary layer will influence the conditional statistics. However, for large values of the threshold in Eq. (6), the probability of the large optical distortions in the LEBU-modified boundary layer is increasingly small. For instance, $Th = 2$ would correspond to larger than $3.4 OPD_{rms}^{(LEBU\ BL)}$-deviation optical events, which happen less than 1%.

The second source of the differences in the wavefronts it that during some events instantaneous SRA fails to properly predict density fluctuations, as pressure and total temperature variations are not small during these events. It has been shown that the pressure fluctuations in shear layers with well-defined vortical structures significantly contribute to the overall aero-optical distortions [17]. If a vortical structure is present, a pressure will be less inside of it due to a balance between the centrifugal and pressure forces, and the optical distortions will be also less than the velocity-predicted ones (leading to the negative differences). On the other hand, if the flow is almost stagnant in some strain-dominated regions, the pressure will be higher in this region, resulting in the positive difference.

Based on this notion it is plausible to assume that a packet of vortical structures in the boundary layer, called a large-scale structure, might have an associated lower pressure region inside. If present, this pressure drop would result in the negative difference between the measured and the SRA-estimated wavefront distortions. The evidence of these shear-layer-type structures has been found in adverse pressure gradient boundary layers, and it was speculated that these structures might be present intermittently in zero-pressure boundary layers [18]. The large-scale structures are located mostly near the wall, which is consistent with the observation that during the negative differences, the conditional u-fluctuations are the largest around $y/\delta = 0.3$, see Figure 10, right.

Unfortunately, the collected velocity fields were relatively noisy, so the pressure fields, computed from the velocity fields, using some known techniques [14, 19,20] were not reliable to make any direct estimation of the pressure and pressure-related density variations inside the boundary layers; more accurate
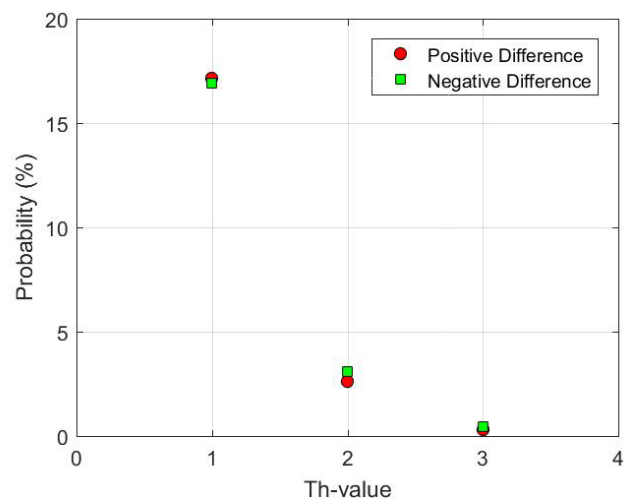

Figure 11. The probability of large positive and negative differences between the actual and the SRA-predicted optical distortions for difference threshold values, defined in Eq. (6).

11

measurements are needed to further study the pressure effect.

The instances where the differences are large are rather infrequent, as shown in Figure 11. So overall, the instantaneous version of SRA can be used most of the time to predict the instantaneous optical distortions in the boundary layers.

V.   Conclusions

Simultaneous measurements of the time-resolved (u-v) velocity field and the overall optical distortions were performed in the subsonic boundary layer using PIV system and the wavefront sensor. The velocity measurements were performed along the wall-normal plane and optical distortions were also measured along the wall-normal direction. The u-fluctuations were used to estimate the aero-optical distortions along the measurement planes, using the instantaneous version of the Strong Reynolds Analogy. The estimated optical distortions were compared with the actual ones to estimate the validity of the instantaneous SRA. The conditional analysis was performed on the velocity field during the large positive and large negative optical aberrations. It was found that while the optical distortions, characterized by OPD, have a symmetric probability distribution, the underlying velocity events or structures are different for positive and negative optical distortions. During the large positive optical distortions the velocity fluctuations primarily reside near the wall, and during the large negative optical distortions the velocity fluctuations were shifted toward negative u-fluctuations primarily in the middle of the boundary layer. Similar asymmetry was observed in the averaged value of the uv-Reynolds shear stress. The shear stress was increased near the wall and suppressed away from the wall during the positive OPDs. During the negative OPDs, the shear stress was significantly increased along the entire boundary layer thickness.

Instances when the velocity-predicted optical distortions differ from the actual optical distortions were also analyzed. Negative differences between the actual and the predicted optical distortions were speculated to be related to the vortical large-scale structures, which create lower-than-ambient pressure fields. Positive differences were thought to be related to the strain-dominant regions with higher-than-ambient pressure fields. Probability of these large differences were found to fairly small. Overall, it was found that the instantaneous SRA correctly predicts the instantaneous aero-optical distortions in the boundary layer most of the time.

The instantaneous SRA relies only on u-fluctuations to predict aero-optical distortions. Indeed, the conditionally-averaged v-fluctuations were found to several times smaller during the large optical distortions, compared to the averaged u-fluctuations. So, rakes of single hot-wires can be used to further study the relation between the instantaneous velocity field and the resulting aero-optical distortions.

Once establishing a statistical link between OPD events and u'- v' statistics, optical measurements can be used in conjunction with traditional velocity measurements to study the large-scale structures and their interaction with near-wall small-scale structures. For instance, by placing the PIV plane parallel to the wall, one can study a spanwise topology of the structure at different y-values during particular optical events. Also, placing the PIV plane near the wall allows one studying near-wall turbulence from PIV along with information about large-scale structures from simultaneous optical data.

References

[1] Marusic, I., McKeon, B. J., Monkewitz, P. A., Nagib, H. M., Smits, A. J. and Sreenivasan, K. R. 'Wall-bounded turbulent flows: recent advances and key issues' *Phys. Fluids*, **22**, 65103, 2010.

[2] Smits, A. J., McKeon, B. J. and Marusic, I. 'High Reynolds number wall turbulence' *Annual Review of Fluid Mechanics*, **43**, pp. 353-375, 2011.

[3] Elsinga, G.E., Scarano, F., Wieneke, B. and Van Oudheusden, BW.," Tomographic particle image velocimetry", *Experiments in Fluids*, **41**(*6*), pp. 933-947, 2006.

[4] Fahringer, T. and Thurow, B., "Tomographic Reconstruction of a 3-D Flow Field Using a Plenoptic Camera", *AIAA Paper 2012-2826*, 2012.

[5] Wang, M., Mani, A., and Gordeyev, S., "Physics and Computation of Aero-Optics", *Annual Review of Fluid Mechanics*, Vol. **44**, pp. 299-321, 2012.

[6] Sutton, G.W., "Effect of turbulent fluctuations in an optically active fluid medium," *AIAA Journal*, **7**(*9*), pp. 1737-1743, 1969.

[7] Gordeyev, S., Smith, A.E., Cress, J.A. and Jumper E.J., "Experimental studies of aero-optical properties of subsonic turbulent boundary layers," *Journal of Fluid Mechanics*, **740**, pp 214-253, 2014.

[8] Morkovin, M.V "Effects of compressibility on turbulent flows," in *Mechanique de la Turbulence* (ed. By A. Favre), CNRS, pp. 367-380, Paris, France, 1962.

[9] Gordeyev, S., Cress, J.A, Smith, A.E. and Jumper. E.J., "Aero-Optical Measurements in a Subsonic, Turbulent Boundary Layer with Non-Adiabatic Walls," *Physics of Fluids*, **27**, 045110, 2015.

[10] S. Gordeyev, A.E. Smith, T. Saxton-Fox and B. McKeon, "Studies of the large-scale structure in adiabatic and moderately-wall-heated subsonic boundary layers, " Paper 7A-3, *9th International Symposium on Turbulence and Shear Flow Phenomena (TSFP-9)*, June 30 - July 3, The University of Melbourne, Australia, 2015.

[11] A. Smith and S. Gordeyev, "Aero-Optical Mitigation of Turbulent Boundary Layers Using Large-Eddy Break-Up Devices," *AIAA Paper 2014-0321*, 2014.

[12] Southwell, W. H., "Wave-front estimation from wave-front slope measurements," *Journal of the Optical Society of America*, **70**(*8*), pp. 998-1006, 1980.

[13] S. Gordeyev, R.M. Rennie, A.B. Cain and T. Hayden, "Aero-Optical Measurements of High-Mach Supersonic Boundary Layers," *AIAA Paper 2015-3246*, 2015.

[14] S. Gordeyev and T.J. Juliano, "Optical Characterization of Nozzle-Wall Mach-6 Boundary Layers," *AIAA Paper 2016-1586*, 2016.

[15] S. Gordeyev, J. Cress and E. Jumper, "Far-Field Laser Intensity Drop-Outs Caused by Turbulent Boundary Layers", *Journal of Directed Energy*, 5(1), pp.58-75, Spring 2013.

[16] J.M Wallace, "Quadrant Analysis in Turbulence Research: History and Evolution," *Annu. Rev. Fluid Mech,* **48**, pp. 131-158, 2016.

[17] Fitzgerald, E.J. and Jumper, E.J. "The optical distortion mechanism in a nearly incompressible free shear layer," *J. Fluid Mech*. **512**, pp. 153–89, 2004.

[18] D.M. Schatzman, and F.O. Thomas, "An experimental investigation of an unsteady adverse pressure gradient turbulent boundary layer: embedded shear layer scaling," in review, *J. Fluid Mech.* 2016.

[19] BW van Oudheusden, "PIV-based pressure measurement," *Meas. Sci. Technol*, **24**, 032001, 2013.

[20] J.F.G. Schneiders, S. Pröbsting, R.P. Dwight, B.W. van Oudheusden and F. Scarano, "Pressure estimation from single‑snapshot tomographic PIV in a turbulent boundary layer," *Experiments in Fluids*, **57**:53, 2016, DOI 10.1007/s00348-016-2133-9.